IEEE Access
Multidisciplinary | Rapid Review | Open Access Journal

Received 21 May 2023, accepted 3 June 2023, date of publication 7 June 2023, date of current version 12 June 2023.

Digital Object Identifier 10.1109/ACCESS.2023.3283576

RESEARCH ARTICLE

Automatic Visual Pit Detection System for Bottom Surface of Cylindrical Lithium Battery

SHAOTAO GUO[1] AND ZEQUAN XING[2]
[1]School of Electric Power, Shenyang Institute of Engineering, Shenyang 110136, China
[2]47th Research Institute of China Electronics Technology Group Corporation, Shenyang 110032, China
Corresponding author: Shaotao Guo (381592719@qq.com)

ABSTRACT The pit on the bottom metal surface is one of the important indicators of cylindrical lithium battery surface defect detection. There are many complex factors in the detection of pit: non-uniform illumination of images, uneven reflection of the metal surface, low surface finishing, stains, rust and scratches. To solve these problems, a method for pit detection based on machine vision is proposed. Firstly, the grayscale distribution curve is extracted along the vertical direction of the bottom metal surface. Secondly, the grayscale difference model which is not sensitive to illumination distribution and noises is used to extract gray discontinuous points in a grayscale distribution curve. According to the reflective feature of the metal surface, the adaptive threshold of discontinuous points extraction is determined based on mean background subtraction. Finally, three feature parameters including gray value features and region features are used as the input of support vector machine (SVM) classifier to train and extract the pit region. The algorithm is evaluated on the self-built image database. The experimental results indicate the non-uniform illumination and uneven reflection have no effect on pit detection. Compared with the related well-established methods, our proposed algorithm can provide a better detection effect—the Recall, Precision and FNR are 0.982, 0.991 and 0.018 respectively.

INDEX TERMS Machine vision, grayscale difference model, cylindrical lithium battery, defect detection, mean background subtraction.

I. INTRODUCTION

Cylindrical lithium battery is widely used in many fields such as instrumentation, transportation and medical equipment. The emergence of the new energy electric vehicle industry has greatly promoted the development of cylindrical lithium batteries. With the increasing demand of users' requirements for cylindrical lithium battery and the aggravation of market competition, surface defect detection is an important process for product quality evaluation [1]. Pit is a serious defect on the bottom metal surface of cylindrical lithium battery, which changes the physical structure of the battery, and endangers the quality of the battery seriously. Therefore, the pit detection is an important index. During the production process, due to the collision or friction between the battery and the production equipment, the external stress on the bottom metal surface of the cylindrical lithium battery exceeds the strength of the material itself, resulting in pits. The actual depth of the pit is greater than 0.1mm. This paper mainly studies the detection of pits on the bottom surface, as shown in Fig. 1.

Pits may appear anywhere on the bottom metal surface. Fig.2 shows two coated lithium battery images with pits. The study object of this paper is a low-contrast image with irregular texture features. These pits are of different sizes, shapes, depths, and orientations due to the different external forces. So, the pits have various imaging effects on different metal surfaces of different reflection properties.

At present, the pit detection of cylindrical lithium battery is mainly implemented manually. This detection approach will fatigue the eyes of the observers, which may lead to lower efficiency and reliability of the defect detection result. Therefore, the detection algorithms based on machine vision are developed gradually. The vision-based algorithms can

The associate editor coordinating the review of this manuscript and approving it for publication was Kumaradevan Punithakumar.

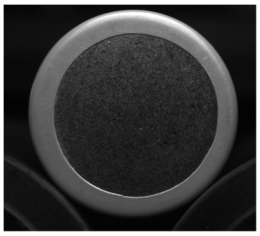

FIGURE 1. The bottom surface of a cylindrical lithium battery.

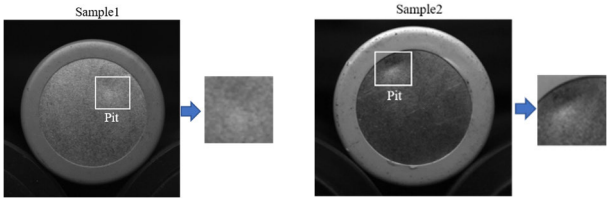

FIGURE 2. Lithium batteries with pits.

offer a more objective assessment than human inspectors. According to the current literatures, there are few researches on the method of detecting pit on the bottom metal surface of cylindrical lithium battery. We perform the literature search of the research on surface detection based on machine vision techniques. Generally, the existing detection methods are categorized into four groups: Statistical, spectral, model-based and machine learning. These researches have achieved good results. However, many researchers have studied the surface detection under the condition that the background is uniform and the defects have high-contrast against the background. The current methods are not applicable to the object studied in this paper, and the specific reasons are as follows.

1) The current methods rely on the gray value of the image [2], [3], [4], and the defect in the uniform background is easy to be extracted. However, when the captured image has uneven background brightness due to the variation of illumination and unsatisfactory environment, the defects with small changes in brightness will be overwhelmed by the brightness of the background. It is difficult to achieve a satisfactory segmentation effect. For example, Liu et al. [4] proposed a new self-reference template guided image decomposition algorithm for strip steel surface defect detection. Combined with the statistical characteristics of a large number of defect-free images, a specific template can be built for each test defect image. Then, a total variation (TV)-based image decomposition algorithm guided by the self-reference template is developed to decompose test image into structural component and textural component. This method depends on the Lagrange multiplier of the constraint selection.

2) The current methods rely on the grayscale difference of adjacent pixels [5], [6], [7], [8]. It will have a good detection effect for the pit whose gray value is much higher or lower than the gray value of its neighborhood. However, it is impossible to separate shallow pits with a small brightness variation range and low brightness contrast with the background, and noise will reduce the accuracy of the algorithm. For example, our research group [8] proposed a pit detection algorithm based on concave-convex curve segment and BP neural network. The temporal averaging and outlier elimination method are used to fuse the six images to obtain the datum image, and the spatial filtering method based on sliding window and Nyquist sampling theorem is used to weaken the influence of noise on the datum image. Finally, a concave-convex curve segment merging algorithm and the BP neural network is used to formulate a detection model to realize pit detection. For the gray level of shallow pits, which is close to the gray level of the background, it is not guaranteed that the minimum point is a real pit, so the detection effect for shallow pits is not good.

3) The current methods describe deficiently about weak signals, and the effectiveness of feature extraction is comparatively low. The current methods are impossible to achieve effective detection of defects with different depths at the same time [9], [10], [11]. In [11], this system employs a baseline convolution neural network (CNN) to generate feature maps at each stage, and then the proposed multilevel feature fusion network (MFN) combines multiple hierarchical features into one feature, which can include more location details of defects.

4) In recent years, the target detection methods based on deep learning have been achieving good performances on automatic defect detection [12], [13], [14] and surface classification [15], [16]. Hu et al. [12] proposes a hybrid multi-dimensional features fusion structure of spatial and temporal segmentation model for automated thermography defects detection. A novel inspection scheme for rail surface defects is presented for limited samples with line-level label, which regards defect images as sequence data and classifies pixel lines [13]. In [14], the VGG19 is firstly used to pre-train the steel surface defect classification task and the corresponding DVGG19 is established to extract the feature images in different layers from defects weight model. Then, the SSIM and decision tree are used to evaluate the feature image quality and adjust the parameters and structure of VGG19. On this basis, a new VSD network is obtained and used for the classification of steel surface defects. However, the detection method based on deep learning needs to collect and label a large number of defective samples. As the enterprises strictly control the rate of defective products, defects are rare in products, which makes deep learning-based defect detection methods are rarely applied in actual detection.

In summary, fewer researches are on the detection method of pit on the bottom surface of cylindrical lithium battery, especially for shallow pits with uneven background brightness and low contrast in the case of non-uniform illumination and uneven reflection. There is still a certain gap between the accuracy of the existing methods and the actual demand in practical application. Aiming

at the above problems, we propose a detection method based on the grayscale difference model with an adaptive threshold and mean background subtraction. This method provides higher robustness to non-uniform illumination and uneven reflection, and effectively improves the effect of pit detection.

The proposed method is as follows: First, Canny, least-square circle fitting and Huber function are used to segment the bottom metal surface. Second, the gray discontinuous points of grayscale distribution curve are extracted based on mean background modeling and grayscale difference model. Then, the candidate pit regions are obtained. Finally, we use gray value features and region features as the inputs of the SVM classifier to exclude the non-pit textures.

The rest of this paper can be divided into the following parts: Section II presents the apparatus system design. Section III analyzes the image characteristics. In Section IV, the proposed pit detection method is detailed. The experiments and results are detailed in Section V. Finally, the conclusion is drawn in Section VI.

II. SYSTEM OVERVIEW

The imaging equipment is mainly composed of four units: transmission unit, image acquisition unit, data processing unit and sorting unit. First, the lithium batteries are put into the feeding trough of the transmission unit, and then they are transferred forward on the roller conveying platform which is composed of two groups of rollers with different diameters under the drive of the motor. As shown in Fig. 3, the movement route of the lithium batteries is marked by the yellow arrows. Then the camera is triggered by the photoelectric switch, encoder and programmable logic controller to acquire an image while the lithium battery is transported to the area of the image acquisition unit. The pit is a non-planar defect, and the illumination in an image is uneven. In order to capture the clearest pit image, the image acquisition unit takes 6 pictures of each battery at an equal angle of 60°. Because the pit detection has slight correlation with color, we use a monochrome area-array CCD camera and a white flat light source in the image acquisition unit. The camera is a XIME MQ013MG-E2 and contains 1280 × 1024 active pixels. The lens is a Computar M2514-MP2. The illuminant is a BTS-100 × 100W-24V side backlight.

The most suitable method for detecting depressions is low-angle illumination. The illumination angle is the angle between the main direction of the light cast by the light source and the direction of the optical axis of the camera's imaging. The lower the illumination angle, the more helpful it is to highlight the pit defect. We conduct the lighting experiments on the self-built image database. The experimental results indicate that the optimal imaging effect can be achieved when the illumination angle is 35°. Next, the images of bottom surface are stored in the computer connected to the imaging equipment. Finally, the computer sends the detection result to the programmable logic controller, and the automatic sorting unit to sort the batteries.

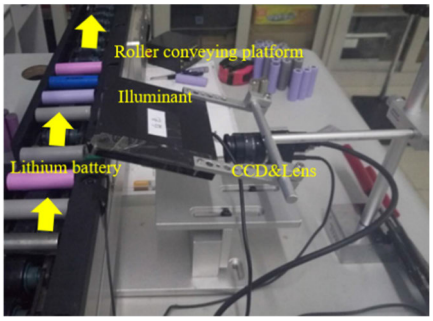

FIGURE 3. The structure of the imaging equipment.

III. IMAGE CHARACTERISTICS ANALYSIS

A. IMAGE CHARACTERISTIC ANALYSIS OF BOTTOM METAL SURFACE

1) GRAYSCALE DISTRIBUTION OF IMAGE

The bottom metal surface is mainly represented by the light and dark speckle texture in vision. Fig. 4 presents two bottom metal surfaces with pit images, two longitudinal scan lines A1 and A2 are drawn in the vertical direction and two transverse scan lines B1 and B2 are drawn in the horizontal direction. A2 and B1 pass through the pit. Observing the three-dimensional grayscale distribution maps, as shown in Fig. 4(b), the gray value range of the bottom metal surface image with various metal materials is different. Each image has a different contrast and brightness. Noise pixels locate in a wide range and the background has a large dynamic intensity range because of non-uniform illumination, low surface finishing and rust.

2) GRAY VALUE CHANGES OF IMAGE ALONG THE VERTICAL DIRECTION

Fig. 4(c) shows the grayscale distribution curves of the longitudinal scan lines on the metal surface. Due to the non-uniform illumination, the curves show a downward trend from top to bottom indicating that the image is getting darker and darker from top to bottom. That is, the image tends to have a large intensity variation along the vertical direction. Because of the low surface finishing and variation of surface reflection, the gray values between adjacent pixels fluctuate with different amplitudes. We can see the fluctuation amplitude of the curve in the pit is slightly larger than that in the neighborhood.

3) GRAY VALUE CHANGES OF IMAGE ALONG THE HORIZONTAL DIRECTION

Fig. 4(d) shows the grayscale distribution curves of the transverse scan lines on the metal surface. We can find that the pit-free areas have a small intensity variation along the horizontal direction. The gray values between adjacent pixels also fluctuates in different amplitude, and the fluctuation amplitude of the pit is slightly larger than that in the neighborhood.

From what has been discussed above, because of the non-uniform illumination, the variation of reflection property of

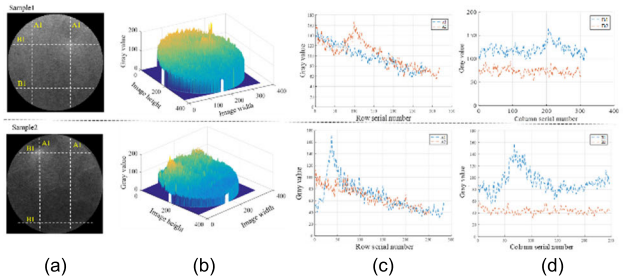

FIGURE 4. Characteristic analysis of bottom metal surface in two samples: (a) Original image, (b) Three-dimensional grayscale distribution, (c) Longitudinal grayscale distribution curve, (d) Horizontal gray distribution curve.

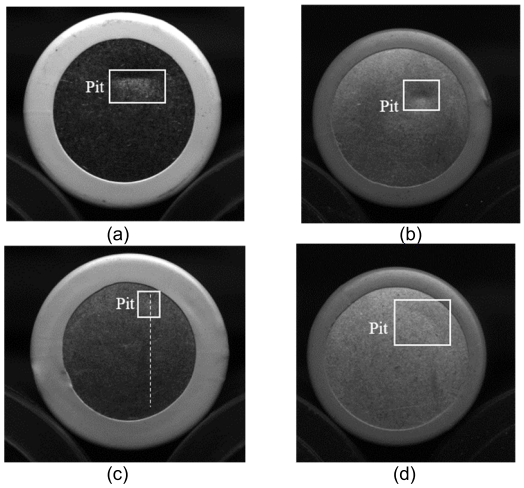

FIGURE 5. Different types of pits: (a) Rectangle deep pit, (b) Ellipse deep pit, (c) Ellipse shallow pit, (d) Arch shallow pit.

the metal surface and rust, the gray distribution of the bottom metal surface is inequal, and the background brightness is inconsistent. The gray level shows irregular distributions in the whole image. Therefore, traditional defect detection methods cannot be directly applied.

From what has been discussed above, because of the non-uniform illumination, the variation of reflection property of the metal surface and rust, the gray distribution of the bottom metal surface is inequal, and the background brightness is inconsistent. The gray level shows irregular distributions in the whole image. Therefore, traditional defect detection methods cannot be directly applied.

B. IMAGE CHARACTERISTIC ANALYSIS OF PIT

The pits do not share common texture or shape features, as shown in Fig. 5. The pit is composed of dense dark patches and bright patches. Dark patches are grayish black and bright patches are bright white in vision. Dark patches are usually not as obvious as bright patches. The pits studied in this paper are mainly divided into deep pits and shallow pits. As shown in Fig. 5(a), 5(b), the deep pits have obvious depressions. The deep pits appear brighter as compared to the pit-free region.

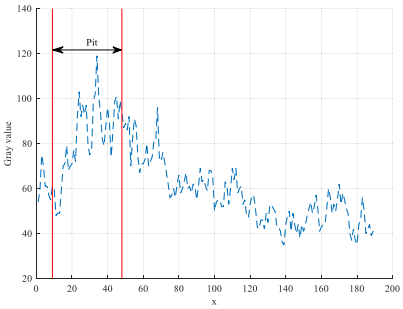

FIGURE 6. Grayscale distribution curve of the shallow pit.

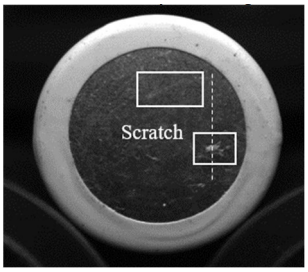

FIGURE 7. The bottom surface image with scratch.

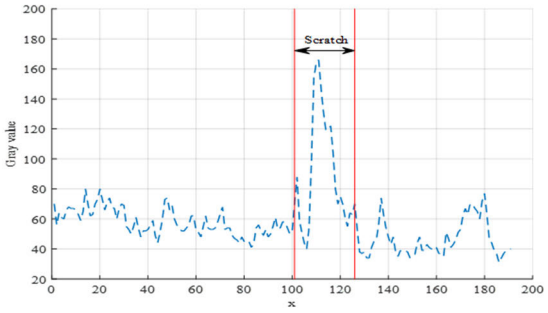

FIGURE 8. Grayscale distribution curve of the scratch.

The shallow pits have a low degree of depression and blurred outline, as shown in Fig. 5(c) and 5(d). There is a slight difference between the shallow pit and its neighborhood, which is hard to distinguish by human eyes. Since the shallow pits are difficult to detect, Fig. 5(c) is used as an example for analysis.

Although the longitudinal and transverse gray distribution curves have obvious fluctuations when they pass through the pit, according to the light source irradiation direction, the longitudinal gray distribution curves can reflect the gray mutation characteristics between dark area and the bright area of pits. The grayscale distribution curve of longitudinal scan line in Fig. 5(c) is shown in Fig. 6. It can be seen that the grayscale contrast between the shallow pit and pit-free area is low. The gray value in the pit area shows a trend of decreasing first and then increasing due to reflection and shadow. We can see the gray value between adjacent pixels in the shallow pit fluctuates slightly, which is similar to that of the pit-free surface.

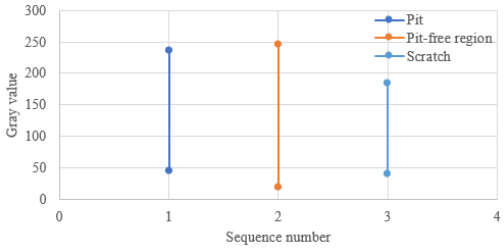

FIGURE 9. Absolute grayscale distribution range of pits, pit-free regions, and scratches.

C. IMAGE CHARACTERISTIC ANALYSIS OF SCRATCH

Due to the influences of material, equipment, and the process craft, the bottom metal surface appears scratches which are not defects. The scratches can seriously interfere with detection. As shown in Fig. 7, these scratches are of different sizes, shapes and orientations, and they are bright white in the image.

The grayscale distribution curve of longitudinal scan line in Fig. 7 is shown in Fig. 8. Similar to the grayscale distribution of pit, scratches have a high grayscale relative to the general metal surface.

The absolute grayscale distribution range of pits, pit-free regions, and scratches in the image dataset, as shown in Fig. 9. It can be seen that their gray distribution ranges overlap each other with little difference. Therefore, it is difficult to detect pit from the background image by the general threshold segmentation algorithm. And there is no obvious distinction between the pit-free area and shallow pit area in the distribution of typical texture feature values after our test.

From what has been discussed above, it is found that there are different amplitude fluctuations on the grayscale distribution curve due to the uneven reflection of the bottom metal surface. The fluctuation of gray distribution curve corresponding to the pits is generally larger than that of the pit-free regions. There is a certain grayscale difference between the pit and the background. Therefore, we propose a pit detection method based on the reflective feature of the bottom metal surface.

IV. PROPOSED METHOD

In this section, we present a pit detection method based on the grayscale difference model and mean background subtraction. The grayscale difference model is a new model proposed in this paper to detect pit texture, which is used to extract gray discontinuous points in gray distribution curve with an adaptive threshold. The proposed detection method of the pit mainly consists of four parts: bottom metal surface image extraction, candidate pit pixels extraction, candidate pit regions segmentation, and non-pit textures exclusion. The flowchart of this method is shown in Fig. 10, and the details are presented in the following sections.

A. BOTTOM METAL SURFACE IMAGE EXTRACTION

The input image not only contains battery, but also has complex background areas such as transmission chains, baffles, etc. These factors might affect the pit detection process. So, the bottom metal surface region should be first extracted in order to improve the execution speed of the algorithm and reduce interference in the subsequent procedures.

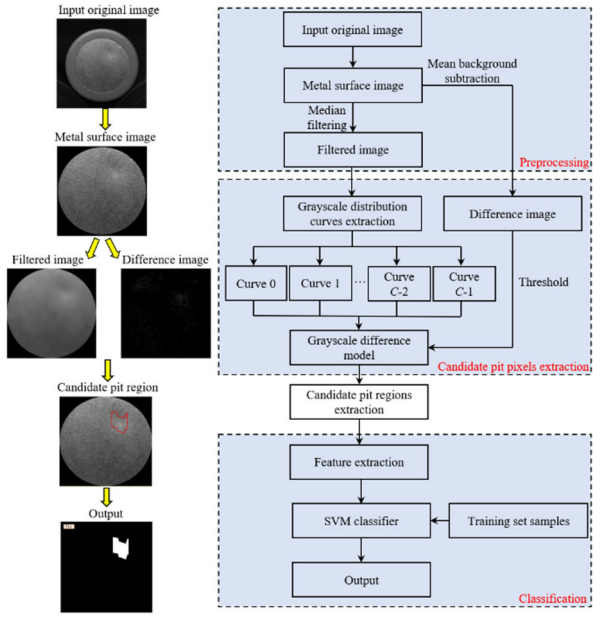

FIGURE 10. Flowchart of the proposed pit detection method.

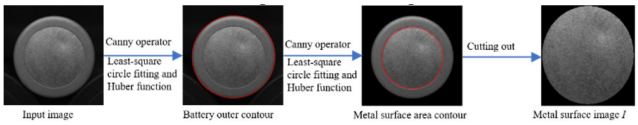

FIGURE 11. Process of bottom metal surface image extraction.

First, according to the characteristic that the battery and background have a certain gray difference, we use Canny operator [17], [18], least-square circle fitting [19], [20], [21] and Huber function [22] to separate the shrink film and metal surface. Then, cutting the smallest surrounding rectangle of the metal surface region of the input image. The above process is shown in Fig. 11. The subsequent procedures are performed on the metal surface image I, containing R rows, C columns.

B. CANDIDATE PIT PIXELS EXTRACTION

1) GRAYSCALE DISTRIBUTION OF IMAGE

Image coordinate system definition: the x-axis represents the row where the pixel is located, the y-axis represents the column where the pixel is located. To suppress noise, we first use a median filter on the image I with a rectangle mask of size 17×17 and returns the filtered image $\bar{I}$. We compare the gray values of the same column of pixels in the image I and the smoothed image $\bar{I}$, as shown in Fig. 12. Then we extract the grayscale distribution curve along the longitudinal direction.

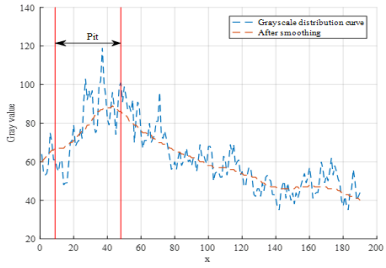

FIGURE 12. Grayscale distribution curves of the shallow pit and the curve after smoothing.

2) GRAYSCALE DIFFERENCE MODEL

After a grayscale distribution curve is extracted, it is divided equally into several segments, each segment contains n data points. The sum of all gray values in the grayscale distribution curve of segment k is defined as:

$$S(k) = G(y, v) \tag{1}$$

where (y, v) represents discrete coordinates as $v \in \{0,1, \ldots, m\text{-}1\}$, m is the data length of each grayscale distribution curve, and $m \leq R$. The constant y is the image column coordinate where the data is located. The value of the grayscale distribution curve at any coordinates (y, v) is denoted $G(y, v)$. And $S(k)$ represents the sum of all gray values in the grayscale distribution curve segment k, satisfying $k \in \{0, 1, 2, \cdots, p\}$, $p \leq (m - n)/2n - 1$. The basic generating principle of the grayscale distribution curve segment is shown in Fig. 13. Each block represents the gray value of pixel position (y, v) in the image.

We use the method of interval subtraction to increase the range of grayscale difference. The grayscale difference model is denoted as:

$$D(k) = S(k + 1) - S(k) \tag{2}$$

where $S(k+1)$ represents the sum of all gray values in the grayscale distribution curve segment $k + 1$. $S(k)$ represents the sum of all gray values in the grayscale distribution curve segment k. $D(k)$ represents the grayscale difference function.

The $D(k)$ of pit region should be positive according to the direction of illumination, and its absolute value should be the maximum value. Therefore, the $D(k)$ of pit region should satisfy:

$$D'(k) = k|[D(k) > 0] \tag{3}$$

$$D_{max}(k) = k|_{\max_{k=0,1,2\ldots,p}} \left[|D'(k)|\right] \tag{4}$$

where $D'(k)$ represents the obtained data sets of positive grayscale difference, $D_{max}(k)$ represents the maximum value in the absolute value of $D(k)$. The fluctuations caused by the uneven reflection of metal surface is eliminated by

$$P(k) \in \begin{cases} \text{true}, & D_{max}(k) > T \\ false, & otherwise \end{cases} \tag{5}$$

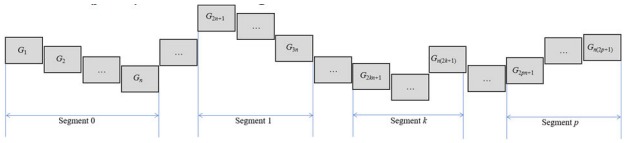

FIGURE 13. Illustration of the grayscale difference model.

where $P(k)$ represents the curve segment k that can be used as candidate pit pixels in each grayscale distribution curve. And T is the grayscale difference threshold whose value will be discussed in the next step.

After obtaining the value of k, the start position and the end position of candidate pixels on the gray distribution curve can be obtained, as in (6), (7).

$$r_s = 2nk + 5 \tag{6}$$

$$r_e = 2n(k + 3) \tag{7}$$

where r_s and r_e represent the start position and end position respectively. $[r_s, r_e]$ is the set of candidate pit pixels. In order to get a whole pit area, the number of pixels is increased. The value of n should be less than half of the height of all pits to obtain all candidate pit pixels and ensure their continuity for subsequent feature screening. According to the statistics of the samples in the dataset, n is set as 6.

3) MEAN BACKGROUND SUBTRACTION

As aforementioned, the grayscale difference threshold T plays a decisive role. The algorithm for selecting optimum threshold value dominates the overall performance of the proposed method. For all images in the dataset, most background pixels take high value similar to the pits, it is difficult to separate pits by a fixed threshold. Therefore, we use an adaptive threshold method. In order to highlight the difference between the pit and the background in gray intensity and reduce the influence of illumination variation and uneven reflection, a background subtraction method based on mean gray value is proposed in this paper.

Background subtraction is a widely used approach for segmenting out objects of interest in the sequence of video frames [23]. The rationale in the approach is that of detecting the moving objects from the difference between the current frame and a reference frame called the ''background model'' [24], which contains no objects of interest. Background subtraction algorithm includes four major steps: preprocessing, background modeling, foreground detection and data validation [25]. Background modeling is the core of background subtraction algorithm, and many different methods have been proposed over the recent years [26], [27], [28], [29], [30], [31].

Inspired by background subtraction, we introduce it to the threshold problem of grayscale difference model. We present mean background subtraction algorithm which remodels each image. Fig. 14 shows the flowchart of mean background subtraction.

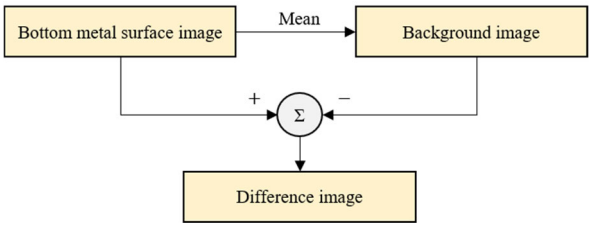

FIGURE 14. The flowchart of mean background subtraction.

First, because the image I tends to have a smaller intensity variation along the y-axis, the mean value of each row of the image I is calculated, and the background image is established according to the mean value. Then, the difference image is obtained by subtracting the image I. The difference image I_d is defined as:

$$I_{bm}(x) = mean(I_y(x)) \tag{8}$$

$$I_d = I - I_{bm} \tag{9}$$

where $I_{bm}(x)$ denotes the image background model of row x, $Iy(x)$ denotes the image I of row x along the y-axis.

The background image I_{bm} is shown in Fig. 15(b). The meaning of the scan lines in Fig. 15 is the same as Fig. 4. The difference image I_d is shown in Fig. 15(c). As shown in Fig. 15(d) and 15(e), the background image has a fixed value along the y-axis, and the change rule along the x-axis is the same as image I, which means it is suitable for background subtraction. The difference image has a uniform background.

4) THRESHOLD SELECTION

Because of the non-uniform illumination and the uneven reflection of the metal surface, a fixed threshold cannot satisfy all the images well. Considering that pit pixels can be regarded as outliers in the gray value distribution of image I_d, we propose an adaptive threshold method based on Chebyshev inequality which can adapt to the statistical characteristics of the detected images. According to Chebyshev inequality [32], in any data set, the proportion of data X that is λ times the standard deviation above the average is at most $1/\lambda^2$:

$$P\{|X - \mu| \geq \lambda\sigma\} \leq 1/\lambda^2 \tag{10}$$

The grayscale difference threshold T is defined as [33]:

$$T = \mu_d + \lambda\sigma_d \tag{11}$$

where μ_d and σ_d denote the mean and standard deviation of gray levels in the image I_d, respectively. The value of λ is determined by the proportion of defects in the image in the dataset and statistics of the experiment.

C. CANDIDATE PIT REGIONS SEGMENTATION

After the above detection of each grayscale distribution curve, the candidate pit region is determined by width of pit. The curve judged as having candidate pit pixels is marked as 1,

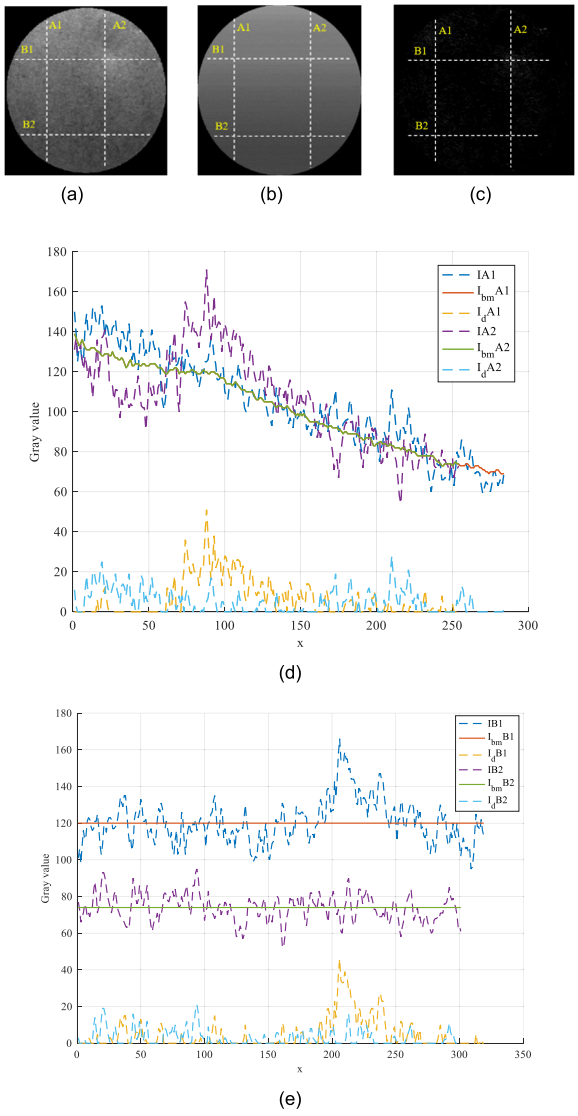

FIGURE 15. Mean background subtraction: (a) Image I, (b) Background image I_{bm}, (c) Difference image I_d, (d) Longitudinal gray distribution curve, (e) Horizontal gray distribution curve.

otherwise it is marked as 0. It is found that the minimum width of pits is 10 pixels, and the maximum width of pits is 178 pixels through the statistics of the samples in the data set. The criteria for determining candidate pit region are defined as:

$$U \in \begin{cases} \text{true}, & 8 < Nc \leq 180 \\ \text{false}, & otherwise \end{cases} \tag{12}$$

where Nc denotes the number of adjacent curves all marked as 1, and U denotes the region that is considered to be candidate pit regions whose location are determined by using (6) and (7).

D. SVM CLASSIFIER

After the candidate pit regions segmentation above, there are still some non-pit textures such as scratches. To exclude

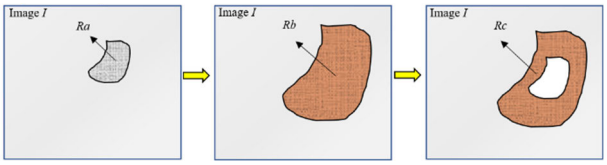

FIGURE 16. Sketch map of absolute neighborhood.

non-pit textures, all target textures are first divided into two classes: (a) pit, (b) noise and scratch. These textures share similar features of human vision system. But they are different in geometric shape and grayscale according to the analysis above. Therefore, the regions to be classified are first mapped back to the region containing the texture in the image I. Then gray value features and region features are used as the input of SVM classifier to train and extract the pit region.

1) FEATURE VECTOR GENERATION

Most of the pixels in the pit region are composed of dark pixels and bright pixels, and the gray value of the bright pixels are higher than that of the neighborhood. Therefore, the gray value of pixels in the pit region is mostly higher than the mean gray value of its neighborhood. We define a texture feature descriptor called absolute neighborhood contrast to denote the contrast between the pit and its neighborhood. As shown in Fig. 16, region Rc is the absolute neighborhood of region Ra. They are adjacent and have no intersection.

Step 1: Use gray-scale morphology [34] to dilate region Ra with a rectangular structuring element to obtain region Rb.

Step 2: Obtain region Rc by using (13). Region Rc contains the remaining points after Rb removes all points in Ra.

$$Rc = (x, y) \,|(x, y) \in Rb \text{ and } (x, y) \notin Ra \tag{13}$$

Step 3: Calculate the absolute neighborhood contrast by using (14).

$$C_{na} = \frac{\lfloor I\,(x, y) - \mu_{Rc} \rfloor}{Aa} \tag{14}$$

where C_{na} is the absolute neighborhood contrast, $I\,(x, y)$ denotes the pixel gray value of the (x, y) coordinates in the image I, μ_{Rc} denotes the mean gray value of region Rc, Aa denotes the area of region Ra. $\lfloor * \rfloor$ represents rounding down.

Since the shallow pits have similar gray levels with background, we further define region gray difference:

$$\alpha = \left[\sum_{q=\Psi(\frac{3}{4}l)}^{l} g\,(q) - \sum_{q=1}^{\Psi(\frac{3}{4}l)-1} g\,(q) \right] \Big/ \sum_{|q=1}^{l} g\,(q) \tag{15}$$

where q denotes a pixel from the region Ra with the gray value $g(q)$, $\Psi(*)$ denotes that $*$ is rounded, l denotes the number of pixels of region Ra.

As shown in Fig. 7, the bright spots of most scratches are concentrated, but pits have an irregular combination of bright and dark spots because of its different reflections due to a certain depth. Therefore, we use a region feature descriptor β which represents the roundness of the region.

Step 1: Cut the classified region Ra of image I, obtain image I'.

Step 2: Segment the image I' by the Otsu's method [35]: All pixels of image I' with gray values greater or equal to T' are selected and obtain the segmented output region Rd.

Step 3: Calculate the roundness of segmented output region Rd by using (16).

$$\beta = 1 - \frac{\sigma_{dc}}{dc} \tag{16}$$

where dc denotes the mean distance between the contour and the center of the region, σ_{dc} denotes the deviation from the mean distance. dc and $\sigma_{Distance}$ are given by

$$dc = \frac{\sum |p - p_i|}{A} \tag{17}$$

$$\sigma_{dc}^2 = \frac{\sum (|p - p_i| - dc)^2}{A} \tag{18}$$

where p denotes the center of the region, p_i denotes the contour pixels of the region, A denotes the area of the contour.

The absolute neighborhood contrast C_{na}, region gray difference α, and roundness β constitute the feature vectors of the target texture $\boldsymbol{F} = [C_{na}, \alpha, \beta]$.

2) PIT EXTRACTION BASED ON SVM CLASSIFIER

SVM adopts the principle based on structural risk minimization and is suitable for solving high-dimensional, small-sample, nonlinear pattern classification problems [36], [37]. In the two classes of target texture, some samples are randomly selected as training samples for SVM $(\boldsymbol{F}_i, \boldsymbol{Y}_i)$, $i = 1, 2, \cdots, u$, where u is the number of training samples and $\boldsymbol{F}_i$ denotes the feature vector of the i-th sample. $\boldsymbol{Y}_i = 1$ indicates that the texture belongs to class 1, $\boldsymbol{Y}_i = -1$ indicates that the texture belongs to class 2. The purpose of training is to build a texture recognition model. After the SVM is trained, it can be used to detect the texture. We use RBF as the kernel function of SVM [38]. Using the RBF kernel can not only realize the linear division of the original training data in the high dimensional space, but also not have a lot of consumption in calculation.

$$K\,(x, z) = e^{-\gamma \|x - z\|^2} \tag{19}$$

where z denotes the center of the kernel function, and γ is the width parameter of the kernel function.

Finally, we set the gray value of the non-pit texture area to 0. The output detection result is obtained as a binary image, in which the white part is the pit.

V. EXPERIMENT AND ANALYSIS

We present the analysis of the parameter λ, and compare the proposed method with well-established methods.

A. IMAGE DATASET

The image dataset of bottom surface of the coated lithium battery is established, which is used to verify the algorithm.

All the images are captured in a real industrial environment. The steps of establishing the dataset are as follows. Firstly, the image acquisition device is used to collect grayscale images of the bottom surface, forming the image dataset SUT-BYE. The resolution of each image is 600 × 540. SUT-BYE contains lithium batteries with different metal surface materials, so there are various imaging effects. To ensure the integrity and clarity of pit, the image acquisition unit takes 6 images of each battery at an equal angle of 60°. Finally, in order to verify the algorithm, the image dataset SUT-BYE is divided into two sub datasets for testing. The image dataset SUT-BYE-1 has 1254 pit defect images, containing 209 lithium batteries, and the image dataset SUT-BYE-2 has 660 pit-free images, containing 110 lithium batteries.

B. EVALUATION METRIC

For further evaluation, a quantitative analysis is performed. The recall (Rc), precision (Pr), and false negative rate (FNR) are three measurement indexes to evaluate the performance of the defect detection. They are defined by

$$\mathrm{Rc} = \frac{TP}{TP + FN} \tag{20}$$

$$\mathrm{Pr} = \frac{TP}{TP + FP} \tag{21}$$

$$\mathrm{FNR} = \frac{FN}{TP + FN} \tag{22}$$

where TP denotes the number of the lithium battery with pits correctly identified as pits, FP denotes the number of the lithium battery with non-pits that are misjudged as pits, FN denotes the number of the lithium battery with pits that are misjudged as non-pits. For the image dataset SUT-BYE-1, in the 6 images of the same battery, the number of images detected as pit is greater than or equal to 1 indicates that the pits are correctly detected. For the image dataset SUT-BYE-2, in the 6 images of the same battery, the number of images detected as pit is greater than or equal to 1 indicates the detection is wrong.

C. ANALYSIS OF PARAMETER

The parameter λ in (11) determines the threshold value T of grayscale difference model and directly affects the Recall and Precision of defects. The selection criterion of λ is that all the pixels in the suspected pit area are included in the set of candidate pit pixels. If the value of λ is too high, the missed detection rate will be high. On the contrary, if the λ is too low, there will be too many misjudgments in the detection results and increase the burden of subsequent detection. Fig. 17 shows the effect of candidate pit pixels extraction results with different values of λ. The white areas denote the extracted candidate pit region. If the value of λ is too low, many background pixels that do not belong to the pit area will be extracted. If the value of λ is too high, the pit cannot be detected. $\lambda = 5.1$ achieves the best performance, since it can not only detect pits but also suppress noise well.

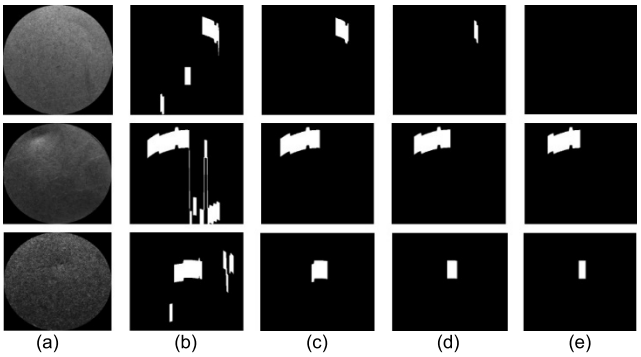

FIGURE 17. Candidate pit pixels extraction results with different values of λ: (a) Surface image, (b) $\lambda = 1.1$, (c) $\lambda = 3.1$, (d) $\lambda = 5.1$, (e) $\lambda = 7.1$.

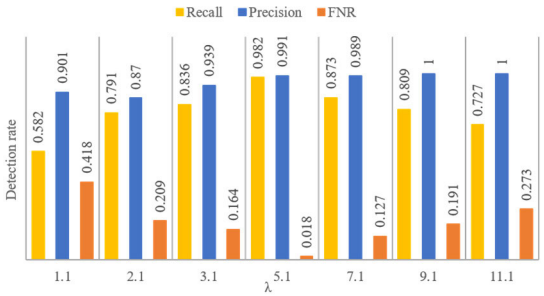

FIGURE 18. Detection performance with different λ.

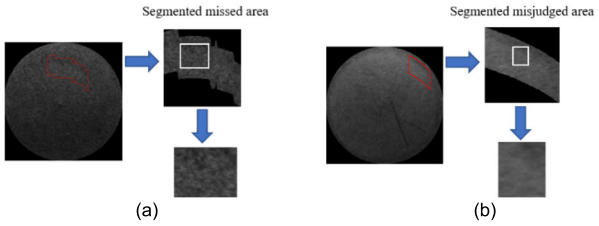

FIGURE 19. Wrongly judged samples in the image dataset: (a) Missed pit texture, (b) Misjudged pit texture.

A detailed comparison of detection performance in our testing dataset is presented in Fig. 18. There is an inverse relationship between Rc and Pr. Generally, Rc increases with the decrease of Pr, so, how to provide a reasonable tradeoff between Recall and Precision is an important indicator to measure a detection system. In order to meet the detection requirements of enterprise, Rc is more important than Pr because a missed pit may result in more loss than a wrongly detected pit. When λ is 5.1, Rc, Pr and FNR are 0.982,0.991, and 0.018 respectively, outperforms others. So, we set $\lambda = 5.1$.

Furthermore, we study the wrongly judged samples, and the typical representatives are shown in Fig. 19. The pits misjudged could be divided into two categories. The first category is shown in Fig. 19(a), the grayscale contrast between the shallow pit and pit-free area is low, which is not obvious in vision, and it causes the loss of region gray difference texture characteristic. The second category

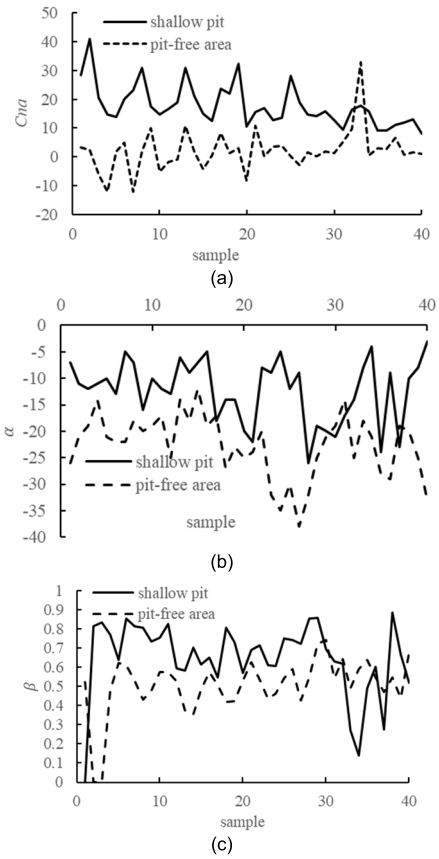

FIGURE 20. Statistics result of feature quantity: (a) The distribution curve of *Cna*, (b) The distribution curve of α, (c) The distribution curve of β.

is shown in Fig. 19(b), it can be seen that there are obvious indentations in the metal surface image due to the film coating. Therefore, there is a significant gray difference in the misjudged area, which is similar to the texture characteristics of the pit, resulting in the wrong judgment.

D. ANALYSIS OF THE FEATURE VECTOR EFFICIENCY

In order to illustrate the effect of the selected feature vectors on the pit detection, the following samples are selected from the image database to analyze the effect of the feature vector on pit texture and non-pit texture. Forty metal surface images with shallow pits and twenty pit-free metal surface images with interference noise are randomly selected. One pit area is manually extracted from each pit defect image, and two different areas are randomly selected from each pit-free image. The absolute neighborhood contrast C_{na}, region gray difference α, and roundness β are calculated respectively. The distribution of each feature vector is shown in Fig. 20.

It can be seen that the three feature vectors can independently describe the corresponding aspects of the pit. They have varying degrees of discernment, but none of these features can uniquely distinguish the pit. It shows that the combination of the three features in this paper are reasonable and can serve as a basis for detecting pit textures.

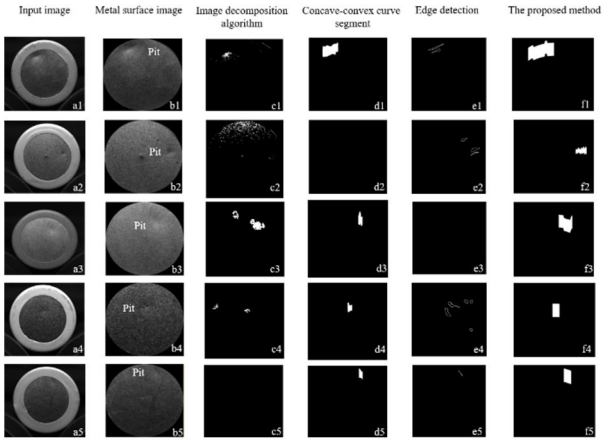

FIGURE 21. Segmentation results on pit defect images.

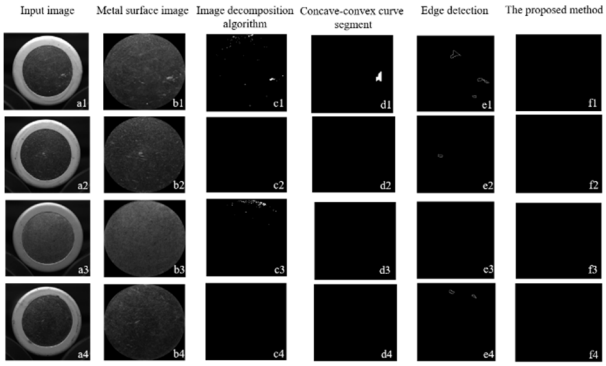

FIGURE 22. Segmentation results on pit-free images.

E. PERFORMANCE COMPARISON WITH RELATED METHOD

To illustrate the detection performance of the proposed algorithm, it is compared with other surface detection methods in the image dataset SUT-BYE: image decomposition algorithm [4], edge detection [7] and concave-convex curve segment method [8]. The parameters of all methods are obtained under the premise that the pit miss rate is the lowest during the experiments. The Lagrange multiplier is set at 2.1 in [4]. The edge detection uses Canny operator with three parameters:5, 5, 15 in [7]. The pit detection results of proposed method and other methods on pit images are shown in Fig. 21. And the segmentation results of proposed method and other methods on pit-free images are shown in Fig. 22. The white areas are the segmentation results.

The pits in Fig. 21 have different depths and sizes. The deep pits are given in Fig. 21(a1) and (a2), the shallow pits are given in Fig. 21 (a3), (a4) and (a5). For deep pits, the other methods can segment most of the pits, but because of non-uniform illumination and uneven reflection, some pit-free areas are also segmented and cannot extract the complete pit region. For shallow pits, the other methods cause missed detection. For example, the method in [7] is limited by the controlling parameters, it cannot accurately

TABLE 1. Comparison of detection performance.

Methods	Rc	Pr	FNR	Time consumption(s)
The method we proposed	0.982	0.991	0.018	0.1907
Image decomposition algorithm [4]	0.873	0.989	0.127	0.0937
Edge detection [7]	0.842	0.809	0.158	0.0856
Concave-convex curve segment [8]	0.871	0.821	0.129	0.0891

detect shallow pits, as shown in Fig. 21(e3) - (e5). This is because these detection methods are limited by local features, they cannot detect pit that has low-contrast against the background. The shallow pits may be identified as background. Similarly, the brighter parts without pits may also be identified as pits. Our method finds the qualified pixels on the grayscale distribution curve which can reflect the small changes in the brightness of shallow pits, so it can accurately and completely segment pits of different depths, as shown in the sixth column of Fig. 21. The threshold selected by our method is higher than the slight amplitude fluctuation on the grayscale distribution curve, so it can eliminate the effects of uniform illumination and uneven reflection.

Fig. 22 shows the segmentation results on pit-free images. Fig. 22(a1) - (a4) contain scratches with high gray values and high contrast with their neighborhood, which interfere with the pit detection and result in false detection in other methods. Because of the more specific features proposed in this paper, the pits and non-pit textures can be effectively distinguished, and the zero-information graph is given, as shown in Fig. 22(f1) - (f4).

Table 1 further demonstrates the comparison of detection performance between our method and the other methods mentioned above. It can be seen that our method obtains better results in Rc, Pr and FNR compared with others. In terms of the time consumption, our method and the other methods are all at the millisecond level. It needs to be mentioned that the proposed method, takes longer execution times than other methods.

To sum up, the experimental results show that other methods do not adequately consider the characteristics of pit, scratch and noise, due to the limitation of local features and template size, resulting in poor detection results. In this paper, we define a grayscale difference model which can truly describe the features of pits. It can segment pits with different depths and sizes completely, and get better segmentation results. Therefore, the proposed algorithm achieves improvement in pit detection accuracy as compared to other methods and is more suitable for shallow pit detection. As long as the contrast between pit and neighborhood can be highlighted on the test image, the algorithm proposed in this paper can be used to detect pits on different surfaces.

VI. CONCLUSION

Based on the analysis of image features and pit features, we propose a new approach for automatically detecting pit defects with low contrast in cylindrical lithium battery images using the grayscale difference model, mean background subtraction and texture analysis, which is fast, robust and accurate. The experimental results have demonstrated that the proposed algorithm can detect shallow pits that has low-contrast against the background more effectively. This will be helpful to promote the defect detection based on machine vision in industry. The main conclusions of this paper are described as follows.

(1) The proposed algorithm in this paper can solve the influence of non-uniform illumination and uneven reflection of the metal surface on pit detection.

(2) The proposed gray value features and region features can effectively distinguish between pits and non-pit textures. This method has universality and practical application value.

(3) The proposed algorithm can be widely used in the detection of weak signal with low contrast between targets and background in the case of non-uniform illumination and uneven reflection.

The algorithm in this paper mainly aims at the on-site detection needs of enterprises, and directly designs a defect detection algorithm based on machine vision that can reflect the characteristics of pits. In future work, we plan to apply this algorithm to other defect detections, further improve the efficiency and robustness against illumination variation.

REFERENCES

[1] Q. Luo, X. Fang, L. Liu, C. Yang, and Y. Sun, "Automated visual defect detection for flat steel surface: A survey," *IEEE Trans. Instrum. Meas.*, vol. 69, no. 3, pp. 626–644, Mar. 2020.

[2] X. Zhou, Y. Wang, Q. Zhu, J. Mao, C. Xiao, X. Lu, and H. Zhang, "A surface defect detection framework for glass bottle bottom using visual attention model and wavelet transform," *IEEE Trans. Ind. Informat.*, vol. 16, no. 4, pp. 2189–2201, Apr. 2020.

[3] X. Ni, H. Liu, Z. Ma, C. Wang, and J. Liu, "Detection for rail surface defects via partitioned edge feature," *IEEE Trans. Intell. Transp. Syst.*, vol. 23, no. 6, pp. 5806–5822, Jun. 2022.

[4] K. Liu, N. Luo, A. Li, Y. Tian, H. Sajid, and H. Chen, "A new self-reference image decomposition algorithm for strip steel surface defect detection," *IEEE Trans. Instrum. Meas.*, vol. 69, no. 7, pp. 4732–4741, Jul. 2020.

[5] J. Wang, Q. Li, J. Gan, H. Yu, and Yang, "Surface defect detection via entity sparsity pursuit with intrinsic priors," *IEEE Trans. Ind. Informat.*, vol. 16, no. 1, pp. 141–150, Jan. 2020.

[6] S. T. Guo and W. Q. Yuan, "A research on the detection method of pit on the cylindrical lithium battery end surface," *Chin. J. Sci. Instrum.*, vol. 43, no. 3, pp. 230–239, 2022.

[7] L. Liu, C. Guo, L. Wang, and H. Mei, "Nondestructive visualization and quantitative characterization of defects in silicone polymer insulators based on laser shearography," *IEEE Sensors J.*, vol. 19, no. 15, pp. 6508–6516, Aug. 2019.

[8] S. T. Guo and W. Q. Yuan, "Pit defect detection of cylindrical lithium battery based on double Gaussian texture filtering template and extreme point Weber contrast," *Acta Electron. Sinica*, vol. 50, no. 3, pp. 637–642, 2022.

[9] G. Cao, S. Ruan, Y. Peng, S. Huang, and N. Kwok, "Large-complex-surface defect detection by hybrid gradient threshold segmentation and image registration," *IEEE Access*, vol. 6, pp. 36235–36246, 2018.

[10] B. Su, H. Chen, Y. Zhu, W. Liu, and K. Liu, "Classification of manufacturing defects in multicrystalline solar cells with novel feature descriptor," *IEEE Trans. Instrum. Meas.*, vol. 68, no. 12, pp. 4675–4688, Dec. 2019.

[11] Y. He, K. Song, Q. Meng, and Y. Yan, "An end-to-end steel surface defect detection approach via fusing multiple hierarchical features," *IEEE Trans. Instrum. Meas.*, vol. 69, no. 4, pp. 1493–1504, Apr. 2020.
[12] B. Hu, B. Gao, W. L. Woo, L. Ruan, J. Jin, Y. Yang, and Y. Yu, "A lightweight spatial and temporal multi-feature fusion network for defect detection," *IEEE Trans. Image Process.*, vol. 30, pp. 472–486, 2021.
[13] D. Zhang, K. Song, Q. Wang, Y. He, X. Wen, and Y. Yan, "Two deep learning networks for rail surface defect inspection of limited samples with line-level label," *IEEE Trans. Ind. Informat.*, vol. 17, no. 10, pp. 6731–6741, Oct. 2021.
[14] S. Guan, M. Lei, and H. Lu, "A steel surface defect recognition algorithm based on improved deep learning network model using feature visualization and quality evaluation," *IEEE Access*, vol. 8, pp. 49885–49895, 2020.
[15] C. Zhao, S. Du, J. Lv, Y. Deng, and G. Li, "A novel parallel classification network for classifying three-dimensional surface with point cloud data," *J. Intell. Manuf.*, vol. 34, no. 2, pp. 515–527, Feb. 2023.
[16] C. Zhao, C. F. Lui, S. Du, D. Wang, and Y. Shao, "An earth mover's distance based multivariate generalized likelihood ratio control chart for effective monitoring of 3D point cloud surface," *Comput. Ind. Eng.*, vol. 175, pp. 1–12, Jan. 2023.
[17] Z. Hocenski, S. Vasilic, and V. Hocenski, "Improved Canny edge detector in ceramic tiles defect detection," in *Proc. 32nd Annu. Conf. IEEE Ind. Electron.*, Nov. 2006, pp. 3328–3331.
[18] J. Canny, "A computational approach to edge detection," *IEEE Trans. Pattern Anal. Mach. Intell.*, vol. PAMI-8, no. 6, pp. 679–698, Nov. 1986.
[19] C. M. Shakarji, "Least-squares fitting algorithms of the NIST algorithm testing system," *J. Res. Nat. Inst. Standards Technol.*, vol. 103, no. 6, p. 633, Nov. 1998.
[20] A. Fitzgibbon, M. Pilu, and R. B. Fisher, "Direct least square fitting of ellipses," *IEEE Trans. Pattern Anal. Mach. Intell.*, vol. 21, no. 5, pp. 476–480, May 1999.
[21] L. Ke, F. Q. Zhou, and G. J. Zhang, "Radius constraint least-square circle fitting method and error analysis," *J. Optoelectron. Laser.*, vol. 17, no. 5, pp. 604–607, May 2006.
[22] P. J. Huber, "Robust regression: Asymptotics, conjectures and Monte Carlo," *Ann. Statist.*, vol. 1, no. 5, pp. 799–821, Sep. 1973.
[23] A. M. McIvor, "Background subtraction techniques," in *Proc. Image Video Comput.*, 2000, pp. 147–153.
[24] M. Piccardi, "Background subtraction techniques: A review," in *Proc. IEEE Int. Conf. Syst., Man Cybern.*, Apr. 2004, pp. 3099–3104.
[25] S. Cheung and C. Kamath, "Robust techniques for background subtraction in urban traffic video," *EURASIP J. Appl. Signal Process.*, vol. 2005, pp. 2330–2340, Jan. 2005.
[26] D. K. Panda and S. Meher, "Detection of moving objects using fuzzy color difference histogram based background subtraction," *IEEE Signal Process. Lett.*, vol. 23, no. 1, pp. 45–49, Jan. 2016.
[27] R. Cucchiara, C. Grana, M. Piccardi, and A. Prati, "Detecting moving objects, ghosts, and shadows in video streams," *IEEE Trans. Pattern Anal. Mach. Intell.*, vol. 25, no. 10, pp. 1337–1442, Oct. 2003.
[28] K. Roy, R. Arefin, F. Makhmudkhujaev, O. Chae, and J. Kim, "Background subtraction using dominant directional pattern," *IEEE Access*, vol. 6, pp. 39917–39926, 2018.
[29] K. K. Hati, P. K. Sa, and B. Majhi, "Intensity range based background subtraction for effective object detection," *IEEE Signal Process. Lett.*, vol. 20, no. 8, pp. 759–762, Aug. 2013.
[30] W. Kim and Y. Kim, "Background subtraction using illumination-invariant structural complexity," *IEEE Signal Process. Lett.*, vol. 23, no. 5, pp. 634–638, May 2016.
[31] L. Wang, W. M. Hu, and T. N. Tan, "A survey of visual analysis of human motion," *J. Comput.*, vol. 25, no. 3, pp. 225–237, 2002.
[32] J. G. Saw, M. C. K. Yang, and T. C. Mo, "Chebyshev inequality with estimated mean and variance," *Amer. Statistician*, vol. 38, no. 2, pp. 130–132, May 1984.
[33] W. Niblack, *An Introduction to Digital Image Processing*. Upper Saddle River, NJ, USA: Prentice-Hall, 1986, pp. 115–116.
[34] J. Serra, "Image analysis and mathematical morphology," *Biometrics*, vol. 39, no. 2, pp. 424–471,1982.
[35] N. Otsu, "A threshold selection method from gray-level histograms," *IEEE Trans. Syst., Man, Cybern.*, vol. SMC-9, no. 1, pp. 62–66, Jan. 1979.
[36] C. Cortes and V. Vapnik, "Support-vector networks," *Mach. Learn.*, vol. 20, no. 3, pp. 273–297, Jan. 1995.
[37] R. Y. Li and L. Cheng, "Building decision tree based on SVM optimal decision surface," *J. Electron. Meas. Instrum.*, vol. 30, no. 3, pp. 342–351, 2016.
[38] L. Lan, Z. Wang, S. Zhe, W. Cheng, J. Wang, and K. Zhang, "Scaling up kernel SVM on limited resources: A low-rank linearization approach," *IEEE Trans. Neural Netw. Learn. Syst.*, vol. 30, no. 2, pp. 369–378, Feb. 2019.

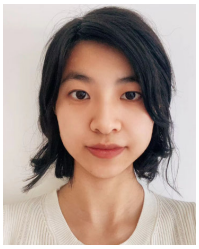

SHAOTAO GUO received the Ph.D. degree from the School of Information Science and Engineering, Shenyang University of Technology, Shenyang, China, in 2022. She is currently a Lecturer with the School of Electric Power, Shenyang Institute of Engineering, Shenyang. Her current research interests include machine vision detection, image processing, and biometric identification.

ZEQUAN XING received the B.S. and M.S. degrees from the Shenyang University of Technology, Shenyang, China, in 2012 and 2015, respectively. He is currently a Senior Engineer with the 47th Research Institute of China Electronics Technology Group Corporation, Shenyang. His current research interests include microelectronics technology, integrated circuit testing, and biometric identification.